

A Thermal Origin for Most Marsquakes

Lei Zhang^{1, 2}, Jinhai Zhang^{1, 2, 3*}, Ross N. Mitchell^{4, 5*}, Peng Cao⁶, Jihang Liu⁷

¹ Key Laboratory of Earth and Planetary Physics, Institute of Geology and Geophysics, Chinese Academy of Sciences, Beijing, China

² Innovation Academy for Earth Science, Chinese Academy of Sciences, Beijing, China

³ College of Earth and Planetary Sciences, University of Chinese Academy of Sciences, Beijing, China

⁴ State Key Laboratory of Lithospheric Evolution, Institute of Geology and Geophysics, Chinese Academy of Sciences, Beijing, China

⁵ University of Chinese Academy of Sciences, Beijing, China

⁶ College of Architecture and Civil Engineering, Beijing University of Technology, Beijing, China

⁷ College of Control Science and Engineering, Bohai University, Jinzhou, Liaoning Province, China

*Corresponding authors: Jinhai Zhang (zjh@mail.iggcas.ac.cn) and Ross Mitchell (ross.mitchell@mail.iggcas.ac.cn)

Key Points:

- Daily and seasonal heat conduction under the InSight landing site is modeled.
- Daily temperature variation over 1 K occurs only within the depth of 25 cm.
- The highest absolute rate of temperature appears around sol 440, coincident with the dominant season of marsquakes observed around sunset.
- Thermal-mechanical simulations indicate that more potential afternoon marsquakes might exist but be covered by the wind noise.
- Most high-frequency and low-magnitude marsquakes are likely thermal in origin.

1 Abstract

2 The thermal response of the martian subsurface due to solar forcing lacks direct
3 measurements. The InSight mission provides the best opportunity to detect the thermal behavior of
4 the subsurface since it was equipped with both air temperature sensors and a subsurface heat flow
5 probe. Here, we model heat conduction under the InSight landing site based on the measured
6 subsurface thermal parameters and air temperature records, which provide insights into heat flow
7 in the martian subsurface. Daily temperature variation over 1 K occurs only within 25 cm under the
8 ground surface. The highest absolute rate of temperature change appears around sol 440, which
9 coincides closely with the season of the dominant number of marsquakes observed around sunset.
10 Thermal-mechanical finite-element method simulations indicate that more potential afternoon
11 marsquakes might exist but be covered by the wind noise. Our results indicate that most
12 high-frequency and low-magnitude marsquakes are likely thermal in origin.

14 Plain Language Summary

15 The mechanism of some marsquakes might not be tectonic in origin, but thermal, related to
16 its large diurnal temperature difference. However, lack of comprehensive near-surface observation
17 makes the thermal investigation challenging. We model the heat conduction beneath InSight based
18 on the measured subsurface thermal parameters and air temperature records. Diurnal and seasonal
19 variations of subsurface temperature and the rate of temperature change are analyzed. Daily
20 temperature variations of >1 K only occur in the top 25 cm of the subsurface. In summer, the
21 absolute rate of temperature change reaches its peak, which is also notably the dominant season of
22 marsquakes observed around sunset. Thermal-mechanical simulations indicate that the
23 heat-induced ground motion is evidently stronger in the daytime than that in the nighttime.
24 Covered by the wind noise, more potential marsquakes might exist in the afternoon through the
25 entire martian year. Our results indicate that high-frequency marsquakes are related to thermal
26 conduction in the top 10 cm of the ground.

28 1 Introduction

29 The daily variation of temperature on Mars can reach up to 80–100 K [*Banfield et al.,*
30 *2020*]. Such a large thermal range can strongly influence both the weather variability and the
31 thermal behavior of the subsurface. Satellite measurements can be used to estimate the thermal
32 parameters from the ground surface to high altitudes [*Ahern et al., 2021; Mellon et al., 2000*], but
33 they can only provide large-scale and intermittent observations. It is difficult to maintain a
34 permanent weather station on the surface of Mars and to perform continuous underground
35 observation, even though both are necessary for understanding the thermal behavior of subsurface
36 materials. The InSight mission was equipped with both an air temperature gauge on the lander
37 [*Spiga et al., 2018*] and a deployable subsurface heat flow probe, the Heat Flow and Physical
38 Properties Package (HP³) [*Spohn et al., 2018*], which provides the best opportunity to detect the
39 thermal behavior of subsurface materials due to the variation of near-surface temperature. The HP³
40 mole successfully bored 20–30 cm deep [*Good et al., 2021*] and performed direct detection on
41 critical thermal parameters of the shallow martian subsurface.

42 Here, we perform a series of numerical simulations to infer the heat conduction process
43 under the InSight landing site, based on the measured subsurface thermal parameters and the air
44 temperature records. We further analyze the daily and seasonal variations of subsurface
45 temperature and the rates of temperature change. Thermal-mechanical coupling finite-element
46 simulations reveal the daily variation of the temperature and the strain in the subsurface. Our
47 results indicate that underground heat conduction on Mars has been critically overlooked in the
48 interpretation of marsquakes.

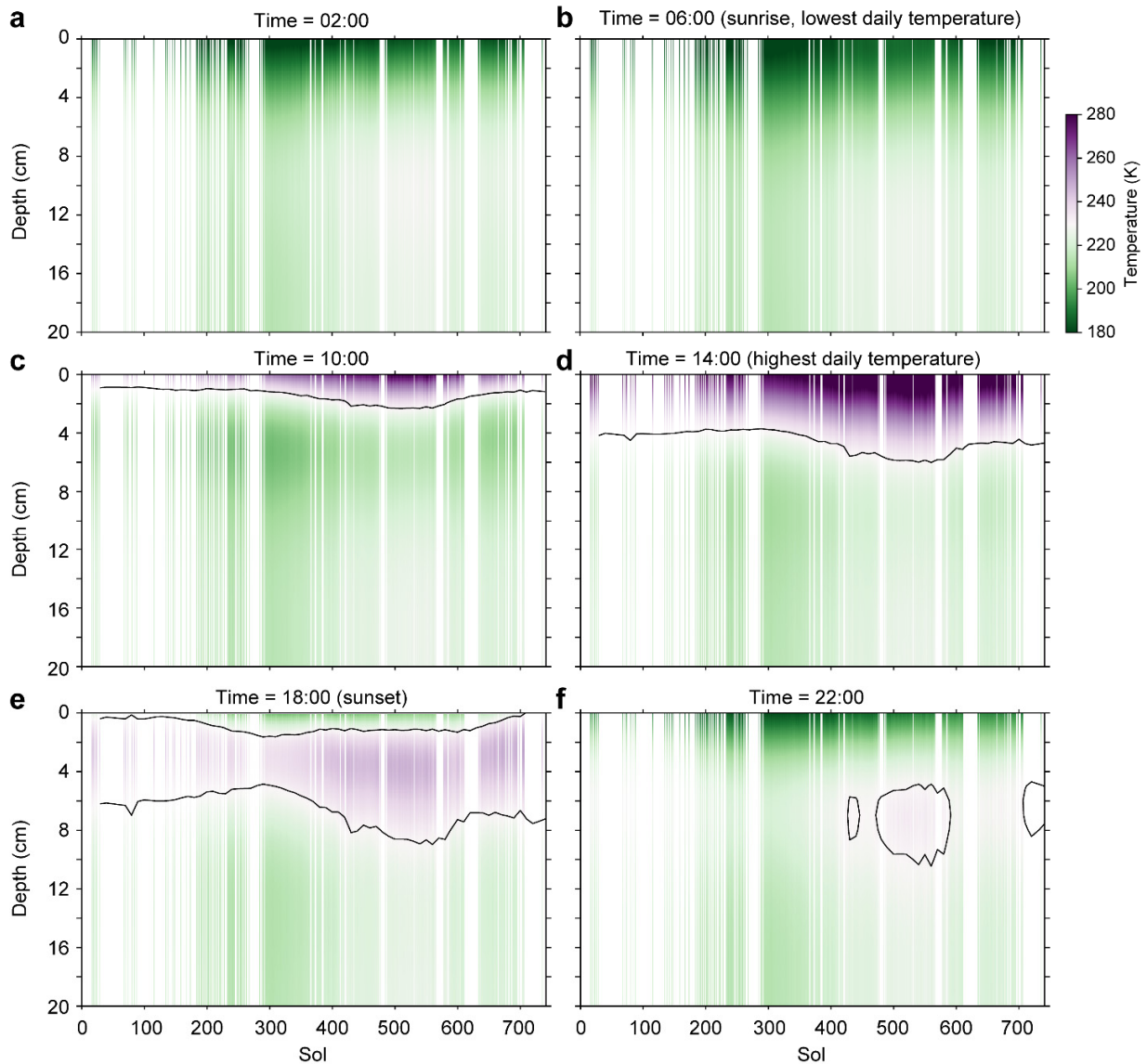
49

50 **2 Diurnal and Seasonal Variations of the Subsurface Heat Conduction Beneath InSight**

51 The heat conduction equation can describe the thermal process of a given model with
52 several controlling parameters (**Text S1**). In our numerical calculations, we use typical values of
53 these parameters obtained from the heating experiments from HP³ [Grott *et al.*, 2021] as follows:
54 soil density $\rho = 1211 \text{ kg m}^{-3}$, specific heat $c = 630 \text{ J kg}^{-1} \text{ K}^{-1}$, and thermal conductivity $k = 0.039 \text{ W}$
55 $\text{m}^{-1} \text{ K}^{-1}$. Thus, the thermal diffusivity $\kappa = k/(\rho c)$ at the InSight landing site can be estimated as
56 $5.1 \times 10^{-8} \text{ m}^2 \text{ s}^{-1}$. The air temperature sensors are on the deck of the InSight lander, $\sim 1 \text{ m}$ over the
57 ground. We correct the air temperature to the ground temperature according to the recorded air
58 temperature and ground temperature from the Martian Climate Database [Forget *et al.*, 1999]
59 (**Text S2; Fig. S1**). Daily subsurface heat conduction calculation results (**Text S3; Fig. S2**) for the
60 annually average sol show that the ground surface (depth of 0 cm) reaches its highest temperature
61 ($\sim 290 \text{ K}$) at $\sim 15:00$ local mean solar time (LMST) and drops to the lowest temperature ($\sim 180 \text{ K}$)
62 slightly before $\sim 06:00$. In contrast, at a depth of $\sim 3 \text{ cm}$, the highest temperature ($\sim 250 \text{ K}$) appears
63 slightly after $\sim 16:00$ and drops to the lowest temperature ($\sim 195 \text{ K}$) slightly after $\sim 06:00$, yielding 1
64 hr and < 1 hr time delays compared to the surface, respectively. At a depth of 7 cm, where the
65 maximum daily variation is only $\sim 15 \text{ K}$, the highest temperature appears at $\sim 19:00$ and the lowest
66 temperature appears at $\sim 11:00$, yielding 4 hr and 5 hr time delays compared to the surface,
67 respectively. Thus, time delays of the lowest and highest temperature ($< 1 \text{ hr cm}^{-1}$) can be seen at
68 different depths. Diurnal temperature variations of over 1 K only occur within the top 25 cm. This
69 indicates that we can focus on the shallowest 25 cm for analyzing the diurnal variations of
70 subsurface temperature, especially for the shallowest 10 cm, below which daily temperature
71 variations are less than 15 K.

72 Similar to the annually averaged data and model, we can further calculate the real-time heat
73 field under the InSight landing site day by day with measured thermal parameters and daily ground
74 temperature. **Figure S3** presents the daily temperature at different depths in the first martian year
75 after InSight landed. The daily ground temperature exhibits several characteristics, such as the
76 lowest daily temperature at $\sim 06:00$ (around sunrise), the highest daily temperature at $\sim 14:00$, and
77 the highest absolute rate of temperature change at $\sim 18:00$ (around sunset). **Figure 1** presents the
78 temperature profile at these moments for each sol. We mark a zone with temperature over $\sim 230 \text{ K}$
79 (black isolines) as the “hot zone” and the other as the “cold zone”. We can see that the “hot zone”
80 at 14:00 has depths within 6 cm, varying from $\sim 4 \text{ cm}$ during sols 0–300 down to $\sim 6 \text{ cm}$ around sol
81 500 (**Fig. 1b**). At 18:00, the “hot zone” is deeper than that at 14:00, varying from $\sim 6 \text{ cm}$ in depth
82 during sols 0–300 down to $\sim 10 \text{ cm}$ around sol 550 (**Fig. 1c**). In sols 230–610, the top of the “hot
83 zone” is 2 cm in depth, which indicates dramatic increases of temperature in this zone.

84



85

86

87

88

89

Figure 1. Temperature as a function of both depth and mission days (sol) at characteristic moments of day. Vertical white spaces indicate data gaps due to solar conjunctions or machine stoppages. Black lines denote the isolines of 230 K.

90

91

3 Correspondence Between Rate of Temperature Change and Ground Motion Around Sunset

92

93

94

95

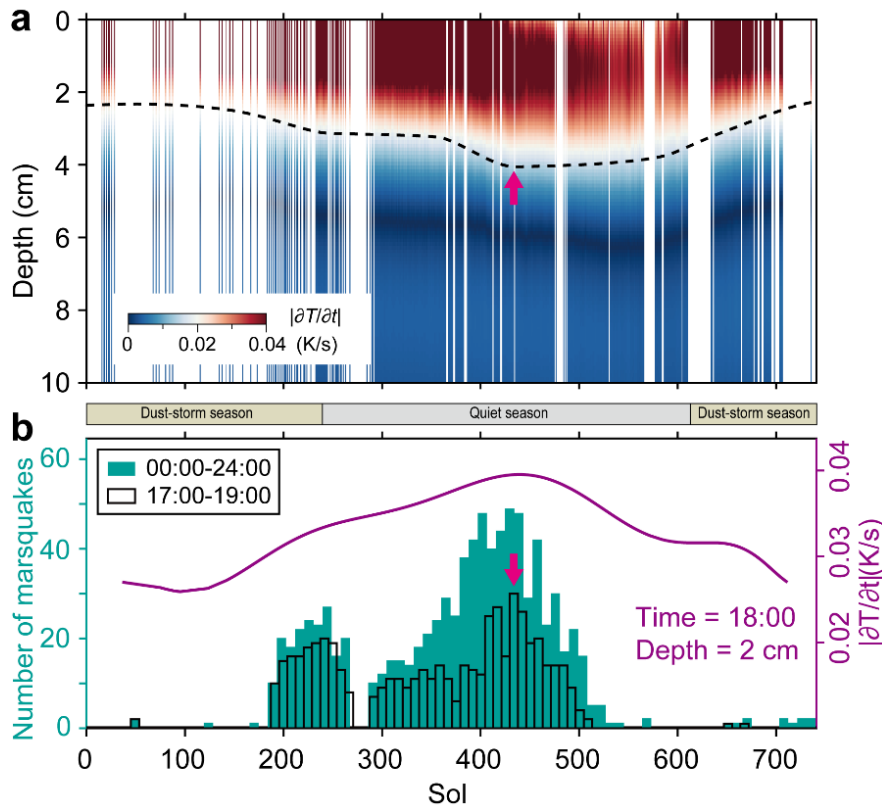
96

97

98

Using seismic data recorded by InSight’s seismic experiment for interior structure (SEIS) [Lognonné *et al.*, 2019] deployed on the ground at the InSight landing site, a number of marsquakes have been detected [Ceylan *et al.*, 2021; Clinton *et al.*, 2021; Giardini *et al.*, 2020]. Strikingly, the timing of marsquakes is highly non-uniform, with no observed diurnal or seasonal dependence (Fig. 2). About 49% of marsquakes occur within a 2 hr time window near sunset (17:00–19:00) and 70% of them occur within a 4 hr time window near sunset (16:00–20:00) (Table S1). Furthermore, nearly all the remaining minority of events occur at nighttime after sunset and

99 twilight (Fig. S4). The strong wind noise precludes the detection of potential weak marsquake
 100 signals during the daytime or in the dust-storm season. Nevertheless, larger magnitude marsquakes,
 101 were they to occur during the windy daytime or dust-storm season, should still be detectable, thus
 102 making their absence conspicuous. That is, if large magnitude marsquakes are tectonic in origin,
 103 they should occur at more or less random times of day and year, assuming that tectonic marquakes
 104 are similar to earthquakes (e.g., *Hao et al. [2019]*). However, only several high quality marsquakes
 105 have been detected in an entire martian year [*Khan et al., 2021*], far lower than the frequency of
 106 moonquakes [*Garcia et al. 2019*].



107 **Figure 2. Rate of temperature change and the ground motion around sunset.** (a) Comparison
 108 between the absolute rate of temperature variation at 18:00 LMST and number of events in
 109 high-frequency family (see below). The dashed line indicates the boundary of $\sim 0.02 \text{ K s}^{-1}$. (b)
 110 Green filled and black framed bars indicate marsquakes during 00:00–24:00 LMST and 17:00–
 111 19:00 LMST, respectively. The purple line is the temperature variation at the depth of 2 cm at
 112 18:00 LMST. Temperature variations at other depths are shown in *Figure S5*. Only marsquakes in
 113 the high-frequency family (HF, VHF, and SHF) [*InSight Marsquake Service, 2021*] are plotted.
 114 See all types of marsquakes in *Figure S6*.

116

117 It is well known that rapid temperature change can cause thermal expansion and
 118 contraction and even cracks in rock, which would change its mechanical properties. It has been
 119 suggested that marsquakes might be related to thermal cracking of the subsurface [*Dahmen et al.,*
 120 *2021*], like thermal quakes on the tectonically dormant Moon [*Duennebieer and Sutton, 1974;*
 121 *Sens-Schönfelder and Larose, 2010*]. Thus, based on our calculated temperature field and the

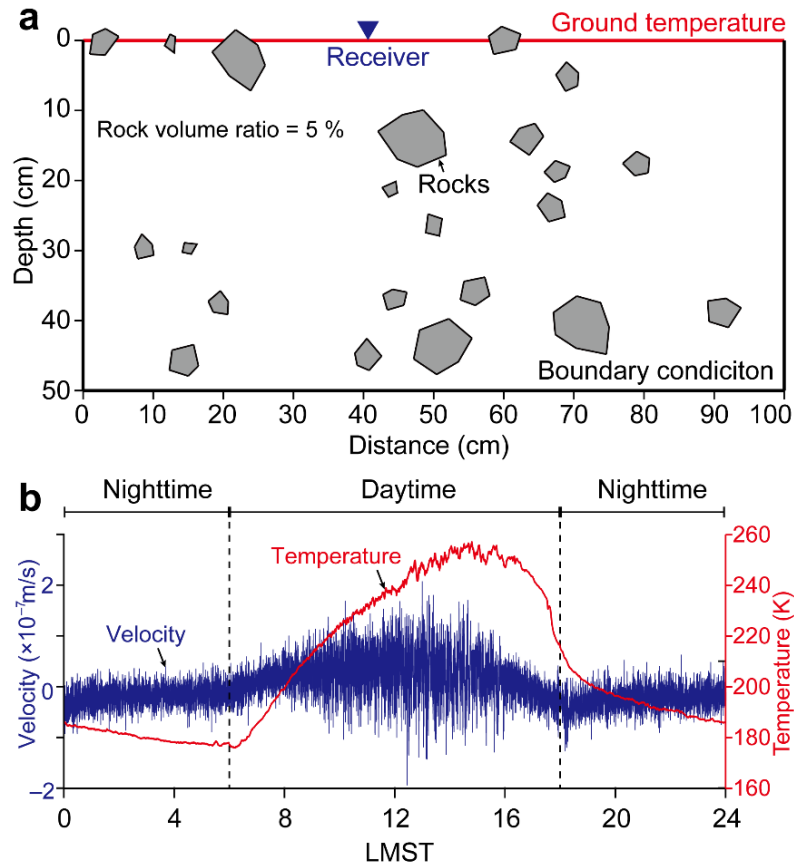
122 InSight marsquake catalog [*InSight Marsquake Service, 2021*], we analyze the correspondence
123 between the seasonal variations in thermal conduction with the occurrences of marsquakes. **Figure**
124 **2** shows the absolute rate of temperature change $|\partial T/\partial t|$ at 18:00 and the number of marsquake
125 events in the high-frequency family [*InSight Marsquake Service, 2021*] during 17:00–19:00. This
126 low-wind time window is the quietest, thus providing the most reliable record of marsquakes (**Fig.**
127 **S4**).

128 It is evident that the absolute rate of temperature variation $|\partial T/\partial t|$ at 18:00 and the
129 number of high-frequency events (high frequency (HF), very high frequency (VHF), and super
130 high frequency (SHF)) are essentially synchronous during an entire martian year (except the
131 dust-storm season), and both reach their peak values at around sol 440 (in summer). It is notable
132 that marsquakes do not occur more frequently during the peak temperature (around sol 540);
133 instead, they occur more frequently around sol 440, corresponding to the peak rate of temperature
134 change. The absolute rate of temperature change on sol 440 was $>0.02 \text{ K s}^{-1}$ within a depth of ~ 4
135 cm (**Fig. 2a**). This indicates that high-frequency events might be related to thermal conduction
136 within only the top several centimeters of the subsurface.

137

138 **4 A Thermal Origin for Most Marsquakes Inferred from Thermal-mechanical Simulation**

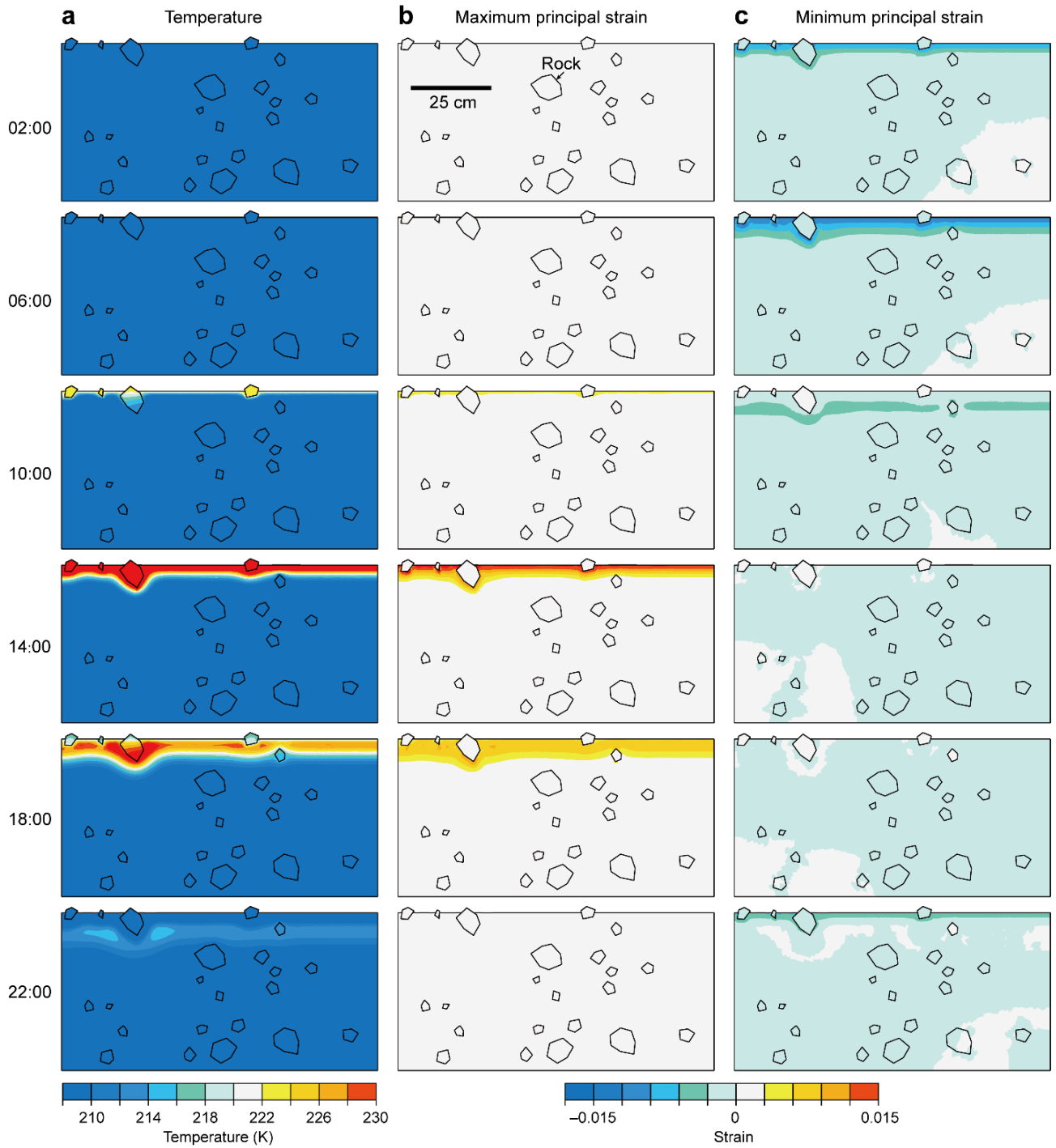
139 Given the low heat conductivity in the martian subsurface, the rock-filled soil with a depth
140 of 50 cm is considered in the simulation. Thus, we use a 2D thermal-mechanical coupling
141 finite-element model (50 cm \times 100 cm) for the subsurface profile (**Fig. 3a**). The displacement
142 boundary condition along the side and bottom boundaries is set as fixed in the normal direction and
143 free in the tangential direction. Given that the thermal conduction dominates mainly in the top 10
144 cm of the subsurface, the top boundary is set as a free surface with corrected ground temperature,
145 while the side and bottom boundaries are set as adiabatic. For the soil at InSight landing site, the S
146 wave velocity, P wave velocity [*Hobiger et al., 2021*] and density [*Grott et al., 2021*] are set as
147 111 m s^{-1} , 200 m s^{-1} , and 1211 kg m^{-3} , respectively; the thermal diffusivity is set as $5.1 \times 10^{-8} \text{ m}^2 \text{ s}^{-1}$,
148 obtained from the measured thermal parameters [*Grott et al., 2021*]; thermal expansion is set as
149 $2.4 \times 10^{-4} \text{ K}^{-1}$ [*Molaro et al., 2017*]. For the rocks buried in the soil (**Fig. 3a**), the S wave velocity,
150 P wave velocity and density are set as 1700 m s^{-1} , 3000 m s^{-1} , and 2760 kg m^{-3} [*Morgan et al.,*
151 *2018*], respectively, derived from terrestrial data obtained for fractured basalt [*Planke et al.,*
152 *1999*]; thermal diffusivity is set as $7 \times 10^{-7} \text{ m}^2 \text{ s}^{-1}$ [*Hartlieb et al., 2016*]; the thermal expansion is
153 set as $1 \times 10^{-5} \text{ K}^{-1}$ [*Molaro et al., 2017*]; and the volume ratio of the filled rocks is set as
154 approximately 5 %.



155
 156 **Figure 3. The 2D thermal-mechanical coupling finite-element model and the simulated**
 157 **ground motion.** (a) The model with a depth of 50 cm and width of 100 cm. The polygons denote
 158 rocks in the soil and the reversed triangle on the ground denotes the receiver of seismic waves. (b)
 159 the input ground temperature, corrected from the InSight temperature record in sol 226 and the
 160 simulated ground motion (vertical velocity) at the receiver of seismic waves.

161 The results show that driven by the diurnal air temperature variation, the ground motion
 162 is evident and highly correlated with the magnitude of temperature changes. The amplitude of
 163 the vertical velocity is evidently larger in the daytime than that in the nighttime (Fig. 3b), which
 164 has similar trend with the measured vertical ground motion by InSight’s SEIS. The peak ground
 165 acceleration of the simulated heat-induced (Fig. S7) is comparable to the average amplitude of
 166 high-frequency marsquake events identified by SEIS [Ceylan et al., 2021] in the sunset (10^{-9} –
 167 10^{-8} m s^{-2}), which indicates that the heat variation might be adequate to induce thermal
 168 marquakes.

169



170

171

172

173

174

Figure 4. Representative snapshots of temperature and strain. (a) Temperature; (b) Maximum principal strain; (c) Minimum principal strain. The 6 rows from the top to the bottom denote the snapshots at 02:00, 06:00, 10:00, 14:00, 18:00 and 22:00 LMST, respectively.

175 Time-varying temperature distribution shows that the subsurface temperature varies
176 mainly within the top ~ 10 cm and is strongly affected by the part-buried rocks (Fig. 4a). In the
177 early morning (e.g., 02:00 and 06:00), the minimum principal strain (Fig. 4c) reaches its lowest
178 values (~ 0.01), which indicates that the subsurface is compressed due to low temperature. In the
179 afternoon (e.g., 14:00 and 18:00), the maximum principal strain (Fig. 4b) reaches its peak values
180 (~ 0.01) in the top ~ 10 cm, which indicates the failure or fracture of the subsurface. This is
181 consistent with the frequently recorded sunset marsquakes. This indicates that more potential
182 afternoon marsquakes might exist but be covered by wind noise before the sunset (e.g., 14:00),
183 during which the maximum strain is even higher than that in the sunset.

184 5 Discussions

185 We simulated the ground motion induced by daily temperature variation in the subsurface.
186 The amplitude of simulated acceleration is $\sim 5 \times 10^{-8}$ m s⁻² in the representative sol (Fig. S7),
187 which is much smaller than that of the observed acceleration by SEIS ($< 10\%$) in the same sol.
188 However, their trends are basically consistent, which are strong in the daytime but weak in the
189 nighttime. These indicate that other sources (e.g., wind) besides temperature variation might
190 dominate the surface ground motion. If the wind was further considered in the simulation, the
191 heat-induced ground motion would be exaggerated and gain a higher amplification on the
192 amplitude of acceleration. More work is needed in the future by considering the coupling process
193 between thermal activity and wind shaking.

194 Our current experiments show that the marsquakes occur at the zone with high strain in
195 the subsurface. Given that the sunset is away from the highest rate of temperature change in the
196 sol, we expect that more potential thermal quakes may exist at the other time periods (such as
197 14:00-16:00 LMST, Fig. 4). However, the wind noise in these times is too strong to detect the
198 weak signals.

199 6 Conclusions

200 Taking the ground temperature and subsurface heat properties observed by InSight as
201 boundary conditions, we performed a series of numerical simulations based on heat conduction
202 equation. From the analyses of subsurface temperature and the rate of temperature change, we
203 infer that the depth of daily temperature variation over 1 K occurs only within 25 cm under the
204 ground surface. This indicates that the strong daily temperature variation (up to 80–100 K) has
205 little influence on the underground materials below this depth. Peak absolute rate of temperature
206 change appears around sol 440 (in summer), which is strikingly coincident with the peak number
207 of marsquakes observed starting at sunset. This temporal correspondence may suggest that the
208 highest absolute rate of temperature change triggers thermal marsquakes. We infer that the thermal
209 marsquakes mainly happen at the depth of < 10 cm, over the zone of daily temperature variation
210 with a threshold as little as 15 K, especially at the uppermost several centimeters with absolute rate
211 of temperature change > 0.02 K s⁻¹. Thermal-mechanical finite-element method simulations
212 indicate that the heat-induced ground motion is evidently stronger in the daytime than that in the
213 nighttime. In the afternoon, the maximum principal strain reaches its peak values in the top ~ 10 cm
214 of the subsurface, which indicates the failure or fracture of the subsurface. The peak ground
215 acceleration of the simulated heat-induced is comparable to the average amplitude of
216 high-frequency marsquake events identified by SEIS in the sunset, indicating that these
217 earthquakes might have thermal in origin.

218 **Acknowledgments**

219 The TWINS (Temperature and Winds for InSight) datasets were downloaded from the
 220 NASA Planetary Data System [[Rodriguez-Manfredi, et al. 2019](#)]. The Marsquake catalog was
 221 obtained from IRIS [[InSight Mars SEIS Data Service, 2019](#)]. Computing resources were provided
 222 by The Supercomputing Laboratory at the Institute of Geology and Geophysics, Chinese Academy
 223 of Sciences (IGGCAS). This work was supported by National Natural Science Foundation of
 224 China (41941002 and 41888101). Comments and suggestions from Brian Shiro highly improved
 225 the manuscript. We thank Xiaofeng Liang for helpful discussions on daily temperature response
 226 of a seismometer deployed in the Taklimakan Desert.

227

228 **References**

- 229 Ahern, A. A., A. D. Rogers, C. S. Edwards, and S. Piqueux (2021), Thermophysical properties
 230 and surface heterogeneity of landing sites on Mars from overlapping Thermal Emission
 231 Imaging System (THEMIS) observations, *Journal of Geophysical Research: Planets*,
 232 *126*(6), e2020JE006713.
- 233 Banfield, D., A. Spiga, C. Newman, F. Forget, M. Lemmon, R. Lorenz, N. Murdoch, D.
 234 Viudez-Moreiras, J. Pla-Garcia, and R. F. Garcia (2020), The atmosphere of Mars as
 235 observed by InSight, *Nature Geoscience*, *13*(3), 190-198.
- 236 Barlow, N. (2014), Mars: An introduction to its interior, surface and atmosphere, *Mars: An*
 237 *Introduction to its Interior*, Cambridge University Press.
- 238 Ceylan, S., J. F. Clinton, D. Giardini, M. Böse, C. Charalambous, M. van Driel, A. Horleston, T.
 239 Kawamura, A. Khan, and G. Orhand-Mainsant (2021), Companion guide to the marsquake
 240 catalog from InSight, Sols 0–478: Data content and non-seismic events, *Physics of the*
 241 *Earth and Planetary Interiors*, *310*, 106597.
- 242 InSight Marsquake Service (2021). Mars Seismic Catalogue, InSight Mission; V7 2021-07-01.
 243 ETHZ, IGP, JPL, ICL, Univ. Bristol. <https://doi.org/10.12686/a12>.
- 244 Clinton, J. F., S. Ceylan, M. van Driel, D. Giardini, S. C. Stähler, M. Böse, C. Charalambous, N.
 245 L. Dahmen, A. Horleston, and T. Kawamura (2021), The Marsquake catalogue from InSight,
 246 sols 0–478, *Physics of the Earth and Planetary Interiors*, *310*, 106595.
- 247 Dahmen, N. L., J. F. Clinton, S. Ceylan, M. van Driel, D. Giardini, A. Khan, S. C. Stähler, M.
 248 Böse, C. Charalambous, and A. Horleston (2021), Super high frequency events: A new class
 249 of events recorded by the InSight seismometers on Mars, *Journal of Geophysical Research:*
 250 *Planets*, *126*(2), e2020JE006599.
- 251 Duennebier, F., and G. H. Sutton (1974), Thermal moonquakes, *Journal of Geophysical*
 252 *Research*, *79*(29), 4351-4363.
- 253 Forget, F., F. Hourdin, R. Fournier, C. Hourdin, O. Talagrand, M. Collins, S. R. Lewis, P. L.
 254 Read, and J. P. Huot (1999), Improved general circulation models of the Martian
 255 atmosphere from the surface to above 80 km, *Journal of Geophysical Research: Planets*,
 256 *104*(E10), 24155-24175.
- 257 Garcia, R. F., et al. (2019), Lunar seismology: An update on interior structure models, *Space Sci*
 258 *Rev*, *215*(8). <https://doi.org/10.1007/s11214-019-0613-y>.
- 259 Giardini, D., P. Lognonné, W. B. Banerdt, W. T. Pike, U. Christensen, S. Ceylan, J. F. Clinton,
 260 M. van Driel, S. C. Stähler, and M. Böse (2020), The seismicity of Mars, *Nature*
 261 *Geoscience*, *13*(3), 205-212.

- 262 Good, A., A. Johnson, and G. Hautaluoma (2021), NASA InSight's 'Mole' ends its journey on
 263 Mars, in <https://www.nasa.gov/feature/jpl/nasa-insight-s-mole-ends-its-journey-on-mars>,
 264 accessed 4 Jan 2021.
- 265 Grott, M., T. Spohn, J. Knollenberg, C. Krause, T. L. Hudson, S. Piqueux, N. Müller, M. P.
 266 Golombek, C. Vrettos, and E. Marteau, et al., (2021), Thermal conductivity of the martian
 267 soil at the InSight landing site from HP³ active heating experiments, *Journal of Geophysical*
 268 *Research: Planets*, 126(7), e2021JE006861.
- 269 Hartlieb, P., M. Toifl, F. Kuchar, R. Meisels, and T. Antretter (2016), Thermo-physical
 270 properties of selected hard rocks and their relation to microwave-assisted comminution,
 271 *Minerals Engineering*, 91, 34-41.
- 272 Hao, J., J. Zhang, and Z. Yao (2019), Evidence for diurnal periodicity of earthquakes from
 273 midnight to daybreak, *National Science Review*, 6(5), 1016-1023.
- 274 Hobiger, M., M. Hallo, C. Schmelzbach, S. Stähler, D. Fäh, D. Giardini, M. Golombek, J.
 275 Clinton, N. Dahmen, and G. Zenhäusern (2021), The shallow structure of Mars at the
 276 InSight landing site from inversion of ambient vibrations, *Nature communications*, 12(1),
 277 1-13.
- 278 InSight Mars SEIS Data Service. (2019). SEIS raw data, Insight Mission. IPGP, JPL, CNES,
 279 ETHZ, ICL, MPS, ISAE-Supaero, LPG, MFSC.
 280 https://doi.org/10.18715/seis.insight.xb_2016.
- 281 Khan, A., S. Ceylan, M. van Driel, D. Giardini, P. Lognonné, H. Samuel, N. C. Schmerr, S. C.
 282 Stähler, A. C. Duran, and Q. Huang (2021), Upper mantle structure of Mars from InSight
 283 seismic data, *Science*, 373(6553), 434-438.
- 284 Lognonné, P., W. B. Banerdt, D. Giardini, W. Pike, U. Christensen, P. Laudet, S. De Raucourt, P.
 285 Zweifel, S. Calcutt, and M. Bierwirth (2019), SEIS: Insight's seismic experiment for
 286 internal structure of Mars, *Space Science Reviews*, 215:12.
 287 <https://doi.org/10.1007/s11214-018-0574-6>.
- 288 Mellon, M. T., B. M. Jakosky, H. H. Kieffer, and P. R. Christensen (2000), High-resolution
 289 thermal inertia mapping from the Mars global surveyor thermal emission spectrometer,
 290 *Icarus*, 148(2), 437-455.
- 291 Molaro, J. L., S. Byrne, and J.-L. Le (2017), Thermally induced stresses in boulders on airless
 292 body surfaces, and implications for rock breakdown, *Icarus*, 294, 247-261.
- 293 Morgan, P., M. Grott, B. Knapmeyer-Endrun, M. Golombek, P. Delage, P. Lognonné, S.
 294 Piqueux, I. Daubar, N. Murdoch, and C. Charalambous (2018), A pre-landing assessment of
 295 regolith properties at the InSight landing site, *Space Science Reviews*, 214(6), 1-47.
- 296 Rodriguez-Manfredi, J.A. et al. (2019), InSight APSS TWINS Data Product Bundle, NASA
 297 Planetary Data System, <https://doi.org/10.17189/1518935>.
- 298 Spohn, T., M. Grott, S. Smrekar, J. Knollenberg, T. Hudson, C. Krause, N. Müller, J. Jänchen, A.
 299 Börner, and T. Wippermann (2018), The heat flow and physical properties package (HP 3)
 300 for the InSight mission, *Space Science Reviews*, 214(5), 1-33.
- 301 Planke, S., E. Alvestad, and O. Eldholm (1999), Seismic characteristics of basaltic extrusive and
 302 intrusive rocks, *The Leading Edge*, 18(3), 342-348.
- 303 Sens-Schönfelder, C., and E. Larose (2010), Lunar noise correlation, imaging and monitoring,
 304 *Earthquake Science*, 23(5), 519-530.
- 305 Spiga, A., D. Banfield, N. A. Teanby, F. Forget, A. Lucas, B. Kenda, J. A. R. Manfredi, R.
 306 Widmer-Schmidrig, N. Murdoch, and M. T. Lemmon (2018), Atmospheric science with
 307 InSight, *Space Science Reviews*, 214(7), 1-64.
- 308